Inorg. Chem. **2008**, *47*, 1803−1814

Forum

Multifrequency Pulsed Electron Paramagnetic Resonance Study of the S_2 State of the Photosystem II Manganese Cluster

Gregory J. Yeagle,[†] M. Lane Gilchrist,[‡] Robert M. McCarrick,[†] and R. David Britt*[,†]

Department of Chemistry, University of California, Davis, One Shields Avenue, Davis, California 95616, and Departments of Chemical Engineering and Biomedical Engineering, The City College of the City University of New York, 140th Street and Convent Avenue, New York, New York 10031

Multifrequency electron spin–echo envelope modulation (ESEEM) spectroscopy is employed to measure the strength of the hyperfine coupling of magnetic nuclei to the paramagnetic ($S = {}^1/_2$) S_2 form of photosystem II (PSII). Previous X-band-frequency ESEEM studies indicated that one or more histidine nitrogens are electronically coupled to the tetranuclear manganese cluster in the S_2 state of PSII. However, the spectral resolution was relatively poor at the ∼9 GHz excitation frequency, precluding any in-depth analysis of the corresponding bonding interaction between the detected histidine and the manganese cluster. Here we report ESEEM experiments using higher X-, P-, and K_a-band microwave frequencies to target PSII membranes isolated from spinach. The X- to P-band ESEEM spectra suffer from the same poor resolution as that observed in previous experiments, while the K_a-band spectra show remarkably well-resolved features that allow for the direct determination of the nuclear quadrupolar couplings for a single $I = 1$ ^{14}N nucleus. The K_a-band results demonstrate that at an applied field of 1.1 T we are much closer to the exact cancelation limit ($\alpha_{iso} = 2\nu_{^{14}N}$) that optimizes ESEEM spectra. These results reveal hyperfine ($\alpha_{iso} = 7.3 \pm 0.20$ MHz and $\alpha_{dip} = 0.50 \pm 0.10$ MHz) and nuclear quadrupolar ($e^2qQ = 1.98 \pm 0.05$ MHz and $\eta = 0.84 \pm 0.06$) couplings for a single ^{14}N nucleus magnetically coupled to the manganese cluster in the S_2 state of PSII. These values are compared to the histidine imidazole nitrogen hyperfine and nuclear quadrupolar couplings found in superoxidized manganese catalase as well as ^{14}N couplings in relevant manganese model complexes.

Introduction

Most of the atmospheric O_2 needed to sustain aerobic life is generated as a byproduct of the light-driven, four-electron oxidation of water catalyzed by photosystem II (PSII). In plants, the active site of PSII is found on the lumenal surface of the thylakoid membrane and is referred to as the oxygen-evolving complex (OEC). The OEC is composed of a tetranuclear manganese cluster, a redox-active tyrosine (Y_Z), and two essential cofactors, Ca^{2+} and Cl^-.[4,5] During catalysis, the OEC cycles through five intermediate states described by the "*S* state" or Kok cycle.[6] These states are designated as S_0-S_4, with S_0 representing the most reduced state and S_4 the most oxidized state. Molecular oxygen is released during the $S_4 \rightarrow S_0$ transition.

Much of our current understanding of the structural makeup of the OEC is based upon numerous spectroscopic, biochemical, and molecular biology experiments performed over the past 3 decades. In addition, relatively recent X-ray crystallographic studies of PSII single crystals have shed additional light on the architecture of the OEC.[7−10] Despite

* To whom correspondence should be addressed. E-mail: rdbritt@ucdavis.edu. Tel: 1-530-752-6377.
[†] University of California, Davis.
[‡] The City College of the City University of New York.

(1) Britt, R. D.; Zimmermann, J. L.; Sauer, K.; Klein, M. P. *J. Am. Chem. Soc.* **1989**, *111*, 3522–3532.
(2) DeRose, V. J.; Yachandra, V. K.; McDermott, A. E.; Britt, R. D.; Sauer, K.; Klein, M. P. *Biochemistry* **1991**, *30*, 1335–1341.
(3) Tang, X. S.; Diner, B. A.; Larsen, B. S.; Gilchrist, M. L., Jr.; Lorigan, G. A.; Britt, R. D. *Proc. Natl. Acad. Sci. U.S.A.* **1994**, *91*, 704–708.
(4) McEvoy, J. P.; Brudvig, G. W. *Chem. Rev.* **2006**, *106*, 4455–4483.
(5) Debus, R. J. *Biochim. Biophys. Acta* **1992**, *1102*, 269–352.
(6) Kok, B.; Forbush, B.; McGloin, M. *Photochem. Photobiol.* **1970**, *11*, 457–475.
(7) Zouni, A.; Witt, H.-T.; Kern, J.; Fromme, P.; Krauss, N.; Saenger, W.; Orth, P. *Nature* **2001**, *409*, 739–743.

10.1021/ic701680c CCC: $40.75
Published on Web 03/10/2008

these efforts, fundamental questions regarding the exact geometric and electronic structure of the manganese cluster and the nature of the protein ligands that coordinate the manganese cluster have yet to be definitively answered.

A significant amount of work has been directed toward understanding the ligand environment of the OEC. Previous Fourier transform infrared (FTIR) and electron paramagnetic resonance (EPR) spectroscopy studies on site-directed mutants of PSII reaction centers from the cyanobacterium *Synechocystis* sp. PCC 6803 have identified the following amino acid side-chain residues as possible ligands to the manganese cluster: Asp-170, Asp-342, Glu-189, Glu-333, His-332, His-337, Glu-354 of CP43 and the carboxy-terminus (Ala-344) of the D1 polypeptide.[11–21] However, more recent FTIR results using D1Asp-170 and D1Glu-189 mutants have suggested that neither is a ligand to a redox-active Mn atom during *S*-state turnover.[22,23] Regardless, these residues have been shown through X-ray crystallography to be in relatively close proximity to the manganese cluster.[9,24]

EPR has served as a primary spectroscopic method for determining the structural and chemical makeup of PSII. Owing to the paramagnetic nature of numerous chemical species (metal centers and radicals) present in the OEC of PSII, conventional continuous-wave (CW)-EPR has been employed to study states S_0–S_3 as well as a number of potential $Y_Z^{\bullet} \leftrightarrow S_x$ "diradical" species.[14,25–29] A recent review by Haddy discusses these CW-EPR signals in detail.[30] CW-EPR has proven to be an indispensable spectroscopic technique for the initial characterization of intermediate *S* states. However, there remain inherent limitations in spectral resolution when studying disordered paramagnetic systems. Such systems tend to suffer from inhomogeneous line broadening as a result of overlapping EPR transitions. The CW-EPR spectrum of the S_2 state of PSII is a classic example of such effects. While seemingly rich in structure, only 18–21 lines of the possible 1296 EPR transitions are visible in the S_2-state "multiline" spectrum.[26] As well, buried beneath this complicated line shape are additional weaker hyperfine (HF) couplings from ligand nuclei within the vicinity of the manganese cluster. Advanced EPR techniques such as electron spin–echo envelope modulation (ESEEM) and electron nuclear double resonance (ENDOR) provide means to overcome the limitations of inhomogeneous broadening and detect and examine these unresolved nuclear couplings. These spectroscopic methods have played significant roles in the furthering our knowledge of the structure, protein ligation, and substrate/inhibitor binding modes of the manganese cluster in the OEC.[31–39]

Pulsed ENDOR spectroscopy provides a powerful method for determining transition-metal and ligand HF couplings. With respect to the electronic structure of the manganese cluster of the OEC in PSII, ^{55}Mn electron spin–echo (ESE) ENDOR spectra of the S_2 and S_0 states have provided detailed information regarding the ^{55}Mn HF values and spin couplings between the paramagnetic Mn ions.[33,40–42] Through simulation of these advanced EPR results, electronic configurations and oxidation states of the Mn ions have been proposed. As such, the manganese cluster in the S_2 state is thought to be composed of a magnetically coupled trimer linked to a monomer with a $Mn^{III}(Mn^{IV})_3$ distribution of oxidation states.[40,43–45]

(8) Kamiya, N.; Shen, J.-R. *Proc. Natl. Acad. Sci. U.S.A.* **2003**, *100*, 98–103.
(9) Ferreira, K. N.; Iverson, T. M.; Maghlaoui, K.; Barber, J.; Iwata, S. *Science* **2004**, *303*, 1831–1838.
(10) Loll, B.; Kern, J.; Saenger, W.; Zouni, A.; Biesiadka, J. *Nature* **2005**, *438*, 1040–1044.
(11) Boerner, R. J.; Nguyen, A. P.; Barry, B. A.; Debus, R. J. *Biochemistry* **1992**, *31*, 6660–6672.
(12) Allahverdiyeva, Y.; Deak, Z.; Szilard, A.; Diner, B. A.; Nixon, P. J.; Vass, I. *Eur. J. Biochem.* **2004**, *271*, 3523–3532.
(13) Campbell, K. A.; Peloquin, J. M.; Diner, B. A.; Tang, X.-S.; Chisholm, D. A.; Britt, R. D. *J. Am. Chem. Soc.* **1997**, *119*, 4787–4788.
(14) Campbell, K. A.; Force, D. A.; Nixon, P. J.; Dole, F.; Diner, B. A.; Britt, R. D. *J. Am. Chem. Soc.* **2000**, *122*, 3754–3761.
(15) Chu, H.-A.; Debus, R. J.; Babcock, G. T. *Biochemistry* **2001**, *40*, 2312–2316.
(16) Debus, R. J.; Campbell, K. A.; Peloquin, J. M.; Pham, D. P.; Britt, R. D. *Biochemistry* **2000**, *39*, 470–478.
(17) Debus, R. J.; Campbell, K. A.; Pham, D. P.; Hays, A.-M. A.; Britt, R. D. *Biochemistry* **2000**, *39*, 62756287..
(18) Debus, R. J.; Campbell, K. A.; Gregor, W.; Li, Z.-L.; Burnap, R. L.; Britt, R. D. *Biochemistry* **2001**, *40*, 3690–3699.
(19) Chu, H.-A.; Hillier, W.; Debus, R. J. *Biochemistry* **2004**, *43*, 3152–3166.
(20) Debus, R. J. *Biochim. Biophys. Acta* **2001**, *1503*, 164–186.
(21) Diner, B. A. *Biochim. Biophys. Acta* **2001**, *1503*, 147163..
(22) Debus, R. J.; Strickler, M. A.; Walker, L. M.; Hillier, W. *Biochemistry* **2005**, *44*, 1367–1374.
(23) Strickler, M. A.; Hillier, W.; Debus, R. J. *Biochemistry* **2006**, *45*, 8801–8811.
(24) Yano, J.; Kern, J.; Sauer, K.; Latimer, M. J.; Pushkar, Y.; Biesiadka, J.; Loll, B.; Saenger, W.; Messinger, J.; Zouni, A.; Yachandra, V. K. *Science* **2006**, *314*, 821–825.
(25) Dismukes, G. C.; Siderer, Y. *Proc. Natl. Acad. Sci. U.S.A.* **1981**, *78*, 274–278.
(26) Dismukes, G. C.; Siderer, Y. *FEBS Lett.* **1980**, *121*, 78–80.
(27) Dismukes, G. C.; Ferris, K.; Watnick, P. *Photobiochem. Photobiophys.* **1982**, *3*, 243–256.
(28) Zheng, M.; Dismukes, G. C. *Inorg. Chem.* **1996**, *35*, 3307–3319.
(29) Campbell, K. A.; Peloquin, J. M.; Pham, D. P.; Debus, R. J.; Britt, R. D. *J. Am. Chem. Soc.* **1998**, *120*, 447–448.
(30) Haddy, A. *Photosynth. Res.* **2007**, *92*, 357–368.
(31) Britt, R. D.; Derose, V. J.; Yachandra, V. K.; Kim, D. H.; Sauer, K.; Klein, M. P. *Curr. Res. Photosynth., Proc. Int. Conf. Photosynth. 8th* **1990**, *1*, 769–772.
(32) Britt, R. D.; Force, D. A.; Campbell, K. A.; Randall, D. W.; Gilchrist, L. M.; Clemens, K. L.; Gingell, D. M.; Peloquin, J. M.; Pham, D. P.; Debus, R. J. *ACS Symp. Ser.* **1998**, *692*, 272–285.
(33) Britt, R. D.; Campbell, K. A.; Peloquin, J. M.; Gilchrist, M. L.; Aznar, C. P.; Dicus, M. M.; Robblee, J.; Messinger, J. *Biochim. Biophys. Acta* **2004**, *1655*, 158–171.
(34) Britt, R. D.; Peloquin, J. M.; Campbell, K. A. *Annu. Rev. Biophys. Biomol. Struct.* **2000**, *29*, 463–495.
(35) Lubitz, W.; Fiege, R.; Bittl, R.; Irrgang, K.-D.; Renger, G. *Bioinorg. Chem.* **1997**, 673–680.
(36) Goussias, C.; Boussac, A.; Rutherford, A. W. *Philos. Trans. R. Soc. London, B* **2002**, *357*, 1369–1381.
(37) Zimmermann, J. L.; Boussac, A.; Rutherford, A. W. *Biochemistry* **1993**, *32*, 4831–4841.
(38) Dorlet, P.; Boussac, A.; Rutherford, A. W.; Un, S. *J. Phys. Chem. B* **1999**, *103*, 10945–10954.
(39) Rutherford, A. W.; Boussac, A.; Faller, P. *Biochim. Biophys. Acta* **2004**, *1655*, 222–230.
(40) Peloquin, J. M.; Campbell, K. A.; Randall, D. W.; Evanchik, M. A.; Pecoraro, V. L.; Armstrong, W. H.; Britt, R. D. *J. Am. Chem. Soc.* **2000**, *122*, 10926–10942.
(41) Kulik, L. V.; Epel, B.; Lubitz, W.; Messinger, J. *J. Am. Chem. Soc.* **2005**, *127*, 2392–2393.
(42) Kulik, L. V.; Lubitz, W.; Messinger, J. *Biochemistry* **2005**, *44*, 9368–9374.
(43) Charlot, M.-F.; Boussac, A.; Blondin, G. *Biochim. Biophys. Acta* **2005**, *1708*, 120–132.

ENDOR (CW-ENDOR, pulsed ENDOR, and ENDOR-induced EPR) studies have additionally been used to study water binding at early *S* states (S_0-S_2) typically comparing results with natural-abundance H_2O versus a ^2H_2O-enriched buffer.[33,46–48] Of note are the Davies pulsed ENDOR and ESEEM experiments by Aznar and Britt.[46] These experiments found two classes of deuterons that exhibit large dipolar HF couplings, suggesting that two H_2O-derived molecules are directly coordinated to the OEC: one to Mn and one possibly to Ca.[33] Further pulsed ENDOR experiments have been applied to study substrate analogues and inhibitor species as well as the magnetic interaction of the tyrosine radical $Y_Z^\bullet$ in the OEC.[13,49–54] Of particular note in these studies is the measure of a dipolar-coupling-derived distance between $Y_Z^\bullet$ and the manganese cluster, as well as a noticeably disordered hydrogen-bonding environment around $Y_Z^\bullet$ in manganese-depleted preparations.[54–56] A distance of 8–10 Å between the manganese cluster and $Y_Z^\bullet$ has been proposed from the recent ENDOR experiments, which is in good agreement with the X-ray crystallography data models.[54,55] For an excellent overview of these ENDOR experiments, we point the reader to reviews by Britt et al. and Lubitz et al.[33,35]

ESEEM spectroscopy has been equally important in studying the OEC in PSII. ESEEM is often more sensitive than ENDOR to small nuclear couplings, and ESEEM spectra can be enhanced by nuclear quadrupolar (NQ) interactions (e.g., ^{14}N, $I = 1$), which may, in turn, broaden ENDOR lines. Ideally, these two pulsed EPR techniques are employed in tandem. ESEEM experiments have targeted substrate water, substrate analogue alcohols, and ammonia binding as well as a number of inhibitors and functionally relevant substitutes for Ca^{2+} such as Sr^{2+}.[1,32,33,57–60] As well, ESEEM spectroscopy has been a valuable tool in studying amino acid coordination to the OEC. ESEEM experiments, in conjunction with ENDOR, have shown that His-189 is coupled to Y_D through a hydrogen bond, and by analogy, His-190 is assumed to be hydrogen-bonded to Y_Z.[54] Two-pulse ESEEM experiments targeting histidine mutants of Asp-170 suggest that Asp-170 mostly likely does not ligate the assembled manganese cluster.[61]

DeRose et al. applied ESEEM spectroscopy to globally labeled ^{15}N and natural-abundance ^{14}N PSII samples from *Synechococcus* and identified a nitrogen coupling to the manganese cluster.[2] This study was done in response to a previous set of experiments, with PSII samples from spinach, targeting ammonia binding to the manganese cluster. The frequency-domain spectra revealed a broad peak at ~5 MHz that was not associated with the ammonia nitrogen.[1] Results from later ESEEM experiments, using PSII core complexes from *Synechocystis* poised in the S_2 state, showed a similar peak observed at ~5 MHz, which disappeared upon labeling of all of the histidine residues with ^{15}N ($I = {}^1/_2$).[3] While these low-frequency X-band experiments have proven worthy in their ability to identify a histidine nitrogen coupling, the lack of ^{15}N modulation and corresponding frequency-domain components provides little detail regarding the ^{15}N HF interaction. As well, the ^{14}N ESEEM data suffered from poor modulation depth, yielding only a single prominent broad peak, giving little insight into the HF and NQ couplings of the corresponding ^{14}N interaction.

A means to resolve these HF and quadrupolar couplings is through multifrequency ESEEM spectroscopy. A number of researchers have found this technique to be a useful method to accurately determine HF and NQ couplings.[62–64] ESEEM spectroscopy relies on the ability to excite both the fully allowed electron-spin transitions and semi-allowed nuclear-spin transitions through a series of microwave pulses. In an ideal case, known as exact cancelation, the time-domain modulation depth is maximized as the transition probabilities of the allowed and semi-allowed become almost equal.[65] This cancelation condition is achieved when the nuclear Zeeman interaction cancels the HF interaction in one electron-spin manifold. Because the nuclear Zeeman interaction is field-dependent, access to multifrequency instrumentation is necessary to achieve the applied field, at a constant *g* value, that leads to cancelation.

To this end, we have applied two- and three-pulse ESEEM spectroscopy, using six microwave frequencies ranging through X-, P-, and K_a-band (9–31 GHz) frequencies, to PSII membranes isolated from spinach. The results of this investigation show a dramatic increase in the time-domain modulation depth at K_a-band frequencies. This increased

(44) Messinger, J. *Phys. Chem. Chem. Phys.* **2004**, *6*, 4764–4771.
(45) Messinger, J.; Robblee, J. H.; Bergmann, U.; Fernandez, C.; Glatzel, P.; Visser, H.; Cinco, R. M.; McFarlane, K. L.; Bellacchio, E.; Pizarro, S. A.; Cramer, S. P.; Sauer, K.; Klein, M. P.; Yachandra, V. K. *J. Am. Chem. Soc.* **2001**, *123*, 7804–7820.
(46) Aznar, C. P.; Britt, R. D. *Philos. Trans. R. Soc. London, B* **2002**, *357*, 1359–1366.
(47) Mino, H.; Ono, T. *Appl. Magn. Reson.* **2003**, *23*, 571–583.
(48) Tang, X. S.; Sivaraja, M.; Dismukes, G. C. *J. Am. Chem. Soc.* **1993**, *115*, 2382–2389.
(49) Gilchrist, M. L., Jr.; Ball, J. A.; Randall, D. W.; Britt, R. D. *Proc. Natl. Acad. Sci. U.S.A.* **1995**, *92*, 9545–9549.
(50) Force, D. A.; Randall, D. W.; Britt, R. D.; Tang, X.-S.; Diner, B. A. *J. Am. Chem. Soc.* **1995**, *117*, 12643–12644.
(51) Tang, X.-S.; Randall, D. W.; Force, D. A.; Diner, B. A.; Britt, R. D. *J. Am. Chem. Soc.* **1996**, *118*, 7638–7639.
(52) Dole, F.; Diner, B. A.; Hoganson, C. W.; Babcock, G. T.; Britt, R. D. *J. Am. Chem. Soc.* **1997**, *119*, 11540–11541.
(53) Diner, B. A.; Bautista, J. A.; Nixon, P. J.; Berthomieu, C.; Hienerwadel, R.; Britt, R. D.; Vermaas, W. F. J.; Chisholm, D. A. *Phys. Chem. Chem. Phys.* **2004**, *6*, 4844–4850.
(54) Diner, B. A.; Force, D. A.; Randall, D. W.; Britt, R. D. *Biochemistry* **1998**, *37*, 17931–17943.
(55) Peloquin, J. M.; Campbell, K. A.; Britt, R. D. *J. Am. Chem. Soc.* **1998**, *120*, 6840–6841.
(56) Dorlet, P.; Di Valentin, M.; Babcock, G. T.; McCracken, J. L *J. Phys. Chem. B* **1998**, *102*, 8239–8247.
(57) Aahrling, K. A.; Evans, M. C. W.; Nugent, J. H. A.; Ball, R. J.; Pace, R. J. *Biochemistry* **2006**, *45*, 7069–7082.
(58) Force, D. A.; Randall, D. W.; Britt, R. D. *Biochemistry* **1997**, *36*, 12062–12070.
(59) Force, D. A.; Randall, D. W.; Lorigan, G. A.; Clemens, K. L.; Britt, R. D. *J. Am. Chem. Soc.* **1998**, *120*, 13321–13333.
(60) Kim, S. H.; Gregor, W.; Peloquin, J. M.; Brynda, M.; Britt, R. D. *J. Am. Chem. Soc.* **2004**, *126*, 7228–7237.
(61) Debus, R. J.; Aznar, C.; Campbell, K. A.; Gregor, W.; Diner, B. A.; Britt, R. D. *Biochemistry* **2003**, *42*, 10600–10608.
(62) Flanagan, H. L.; Singel, D. J. *Chem. Phys. Lett.* **1987**, *137*, 391–397.
(63) Flanagan, H. L.; Gerfen, G. J.; Singel, D. J. *J. Chem. Phys.* **1988**, *88*, 20–24.
(64) Reijerse, E. J.; Tyryshkin, A. M.; Dikanov, S. A. *J. Magn. Reson.* **1998**, *131*, 295–309.
(65) Mims, W. B. *Phys. Rev. B* **1972**, *5*(3), 2409–2419.

modulation depth correlates directly with well-resolved frequency-domain spectra and thus gives greatly increased insight into the nitrogen HF and NQ couplings.

Theory

The S_2-state multiline signal of PSII arises from a $S = {}^1/_2$ ground spin state.[30] Couplings to an ^{14}N nucleus with nuclear spin $I = 1$ lead to the following spin Hamiltonian:

$$\hat{H} = \beta_e \hat{B} \cdot \mathbf{g} \cdot \hat{S} - g_n \beta_n \hat{I} \cdot \hat{B} + \hat{S} \cdot \mathbf{A} \cdot \hat{I} + \hat{I} \cdot \mathbf{P} \cdot \hat{I} \qquad (1)$$

Here, the first term represents the electronic Zeeman interaction. The second term is the nuclear Zeeman interaction. $\mathbf{g}$ is the electronic g tensor. g_n is the nuclear g value. β_e and β_n are the Bohr and nuclear magnetons, respectively. $\hat{B}$ is the external magnetic field vector.

The third term represents the interaction between the electron and nuclear spins, or HF interaction, where $\mathbf{A}$ is the HF interaction tensor with principal values A_{xx}, A_{yy}, and A_{zz}. This term is often decomposed into two separate interactions: an isotropic Fermi contact term, α_{iso}, and an orientation-dependent anisotropic dipolar term, $\tilde{\alpha}_{dip}$:

$$\mathbf{A} = \alpha_{iso} \tilde{I} + \tilde{\alpha} \qquad (2)$$

where $\tilde{I}$ is a unitary identity matrix. In the point-dipole limit, with an axially symmetric HF tensor, where $A_{xx} = A_{yy} \neq A_{zz}$, the HF interaction has principal values

$$(\alpha_{iso} - \alpha_{dip}),\ (\alpha_{iso} - \alpha_{dip}),\ (\alpha_{iso} + 2\alpha_{dip})$$

where α_{dip} has a magnitude described by

$$\alpha_{dip} = (g g_n \beta_e \beta_n) \frac{1}{r^3} \qquad (3)$$

where r is the relative distance between the electron and the nucleus.

The last term in eq 1 is the NQ interaction tensor, $\mathbf{P}$. For nuclei with $I > {}^1/_2$, such as the $I = 1$ ^{14}N nucleus, there exists a nonspherical charge distribution that interacts with any electric field gradient at the nucleus. This creates the NQ interaction. This term is traceless and can be further expressed as

$$\hat{I} \cdot \mathbf{P} \cdot \hat{I} = \frac{e^2 q_{zz} Q}{4I(2I-1)} [(3\hat{I}_z^2 - I(I+1)^2) + \eta(\hat{I}_x^2 - \hat{I}_y^2)] \qquad (4)$$

where Q is the NQ coupling constant, eq_{zz} is the electric-field gradient at the nucleus along the principal z axis, and η is the asymmetry parameter defined by

$$\eta = \left| \frac{q_{xx} - q_{yy}}{q_{zz}} \right|$$

The terms described above are used to derive the modulation functions and amplitudes, as well as the HF and NQ frequencies that manifest themselves in the ESEEM spectrum.

In the limit of exact cancelation, and specifically when a NQ interaction is present, the modulation signal is composed of distinct nuclear frequencies from the two electron-spin manifolds. In one electron-spin manifold, the effective magnetic field approaches zero as the nuclear Zeeman and HF interactions cancel. As a result, the modulation frequencies correspond to the zero-field NQ transition frequencies:

$$\nu_0 = \frac{1}{2}\eta e^2 qQ, \quad \nu_- = \frac{1}{4}(3-\eta) e^2 qQ, \quad \nu_+ = \frac{1}{4}(3+\eta) e^2 qQ \qquad (5)$$

In the other spin manifold, the effective magnetic field results from the sum of the nuclear Zeeman and HF interactions. Corresponding "Zeeman-like" single (ν_{SQ}) and double (ν_{DQ}) quantum frequencies are manifested in the modulation signal. However, the ν_{SQ} transition frequencies are broadened by HF and NQ anisotropy to first order and thus appear unresolved in most powder-pattern-averaged X-band ESEEM spectra.[64] In cases where the effective field is much greater or much smaller than the NQ couplings, resolution of such ν_{SQ} transitions can be apparent.[66,67] The ν_{DQ} transition frequencies are broadened only to second order by such anisotropies and thus are typically resolved in most ESEEM experiments. In these cases, ν_{DQ}, in the limit of isotropic HF coupling, approaches an upper limit frequency:[67,68]

$$\nu_{DQ} = 2\left[\left(\nu_1 + \frac{|\alpha_{iso}|}{2}\right)^2 + \frac{(e^2qQ)^2}{16}(3+\eta^2)\right]^{1/2} \qquad (6)$$

The above equations allow for direct spectral analysis and provide the basic foundation for simulating experimental ESEEM spectra.

Materials and Methods

Sample Preparation. PSII membranes were prepared from spinach according to the method of Berthold et al. with subsequent modifications described by Campbell et al.[69–71] Prior to the final buffer treatment, an aliquot of the sample preparation was taken for activity measurements. The samples were then resuspended in SMNCE buffer, containing 0.4 M sucrose, 15 mM NaCl, 5 mM $CaCl_2$, 1 mM ethylenediaminetetraacetic acid, and 50 mM 2-(*N*-morpholino)ethanesulfonic acid at pH 6.0. In order to exclusively generate the $g = 2$ multiline S_2-state signal, the final buffers contained 3% ethanol by volume.[72] The samples were centrifuged for 30 min at 38 000*g* prior to sample tube loading. The final chlorophyll concentration for each sample ranged from 12 to 18 mg of chlorophyll per mL. A Clark-type O_2 electrode was used to monitor the oxygen evolution activity of the PSII membranes in the presence of 300 μM 2,6-dichloro-*p*-benzoquinone as the terminal electron acceptor. The obtained rates were 600–800 μM O_2 per mg of chlorophyll per hour.

Sample Illumination. X-band EPR samples, in 3.8 mm quartz EPR tubes, were advanced to the S_2 state by illumination in a nonsilvered Dewar for 10 min at 195 K (dry ice/ethanol). P-band samples were illuminated with white light through fiber-optic cables

(66) Mims, W. B.; Peisach, J.; Davis, J. L. *J. Chem. Phys.* **1977**, *66*, 5536–5550.
(67) Flanagan, H. L.; Singel, D. J. *J. Chem. Phys.* **1987**, *87*, 5606–5616.
(68) Astashkin, A. V.; Dikanov, S. A.; Tsvetkov, Y. D. *J. Struct. Chem.* **1984**, *35*, 45–55.
(69) Berthold, D. A.; Babcock, G. T.; Yocum, C. F. *FEBS Lett.* **1981**, *134*, 231–234.
(70) Ford, R. C.; Evans, M. C. W. *FEBS Lett.* **1983**, *160*, 159–164.
(71) Campbell, K. A.; Gregor, W.; Pham, D. P.; Peloquin, J. M.; Debus, R. J.; Britt, R. D. *Biochemistry* **1998**, *37*, 5039–5045.
(72) Zimmermann, J. L.; Rutherford, A. W. *Biochemistry* **1986**, *25*, 4609–4615.

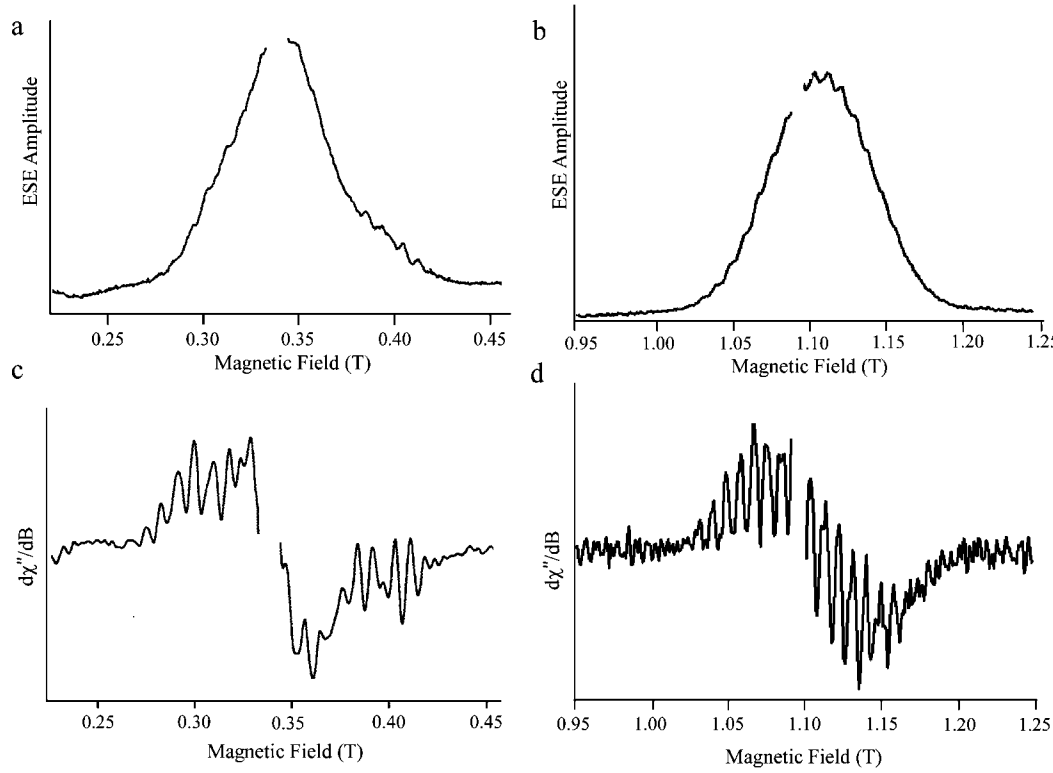

Figure 1. Two-pulse X- and K_a-band ESE field-swept "light-minus-dark" normalized difference spectra of the S_2-state multiline signal in PSII. Panel a shows the X-band field sweeps, and panel c shows the corresponding numerical field derivative. Panel b shows the K_a-band field sweeps, and panel d shows the corresponding numerical field derivative. Instrument settings. X-band: $\nu_{MW} = 9.3607$ GHz, $\pi/2$ pulse = 30 ns, $\tau = 210$ ns, magnetic field increment = 0.5 mT, repetition time = 15 ms, temperature = 4.2 K. K_a-band: $\nu_{MW} = 30.757$ GHz, $\pi/2$ pulse = 30 ns, $\tau = 220$ ns, magnetic field increment = 1.0 mT, repetition time = 5 ms, temperature = 4.5 K.

directed through holes in the wall of the Mims cavity resonator.[73,74] This illumination was carried out in a Janis variable-temperature cryostat, where the temperature was maintained by a Lake Shore temperature controller at 195 K before cooling to the observation temperature of 4.2 K. K_a-band samples, in 2.5 mm quartz EPR tubes, were illuminated in a Dewar for 8 min at 195 K by flowing N_2 gas through a heat exchanger submerged in liquid N_2. The temperature of the N_2 gases was monitored at the sample position with a thermocouple.

EPR Spectroscopy. X-, P-, and K_a-band ESEEM experiments were performed at the CalEPR center at University of California, Davis (http://brittepr@ucdavic.edu), at temperatures of 4.2 and 4.5 K, respectively, on two home-built pulsed EPR spectrometers described elsewhere.[75,76] These experiments were performed at field positions corresponding to a constant g value, over six microwave frequencies: X-band (9.505, 9.749, and 10.955 GHz), P-band (13.530 and 15.517 GHz), and K_a-band (30.757 GHz) light-minus-dark difference spectra, generated in order to isolate the light-induced $g = 1.98$ multiline signal, result from subtracting the dark-adapted PSII spectra from the spectra obtained following continuous white light illumination at 195 K.

Two-pulse or primary spin–echo-detected EPR (ESE-EPR; $\pi/2-\tau-\pi-$primary echo) was performed by integrating the spin–echo for a fixed τ value as a function the external magnetic field. Two-pulse time-domain ESEEM experiments were performed at a fixed magnetic field by monitoring the spin–echo as a function of the interpulse time τ in the primary echo sequence. Three-pulse or stimulated echo time-domain ESEEM experiments were performed at a fixed τ and magnetic field by incrementing T in the stimulated echo sequence ($\pi/2-\tau-\pi/2-T-\pi/2-$simulated echo). Specific spectrometer parameters are described in the figure captions. Fourier transformation of the time-domain signals yields the corresponding frequency-domain spectra. Reconstruction of the experimental "dead time" was analyzed by the cosine Fourier backfill method described by Mims.[77] ESEEM simulations were calculated with a Matlab written matrix diagonalization routine, based on the procedure of Mims.[78]

Results

ESE Field-Swept Spectra. Parts a and b of Figure 1 show the S_2-state ESE field-swept spectra at X- and K_a-band microwave frequencies, respectively. For a comparison to the field-modulated derivative CW-EPR spectra, parts c and d of Figure 1 show the corresponding numerical derivatives with respect to the field. Note that, in all panels of Figure 1, the $Y_D^\bullet$ signal has been excised. The absorption spectra in Figure 1a,b show partially resolved ^{55}Mn HF structure attributed to the four ^{55}Mn nuclei that make up the OEC. A notable change going up in frequency to the K_a band is the upfield shift of the "multiline" signal with respect to that of $Y_D^\bullet$. This shift is beneficial in allowing for ESEEM experi-

(73) Mims, W. B. *Rev. Sci. Instrum.* **1974**, *45*, 1583–1591.
(74) Sturgeon, B. E.; Ball, J. A.; Randall, D. W.; Britt, R. D. *J. Phys. Chem.* **1994**, *98*, 12871–12883.
(75) Sturgeon, B. E.; Britt, R. D. *Rev. Sci. Instrum.* **1992**, *63*, 2187–2192.
(76) Stich, T. A.; Lahiri, S.; Yeagle, G.; Dicus, M.; Brynda, M.; Gunn, A.; Aznar, C.; DeRose, V. J.; Britt, R. D. *Appl. Magn. Reson.* **2007**, *31*, 321–341.
(77) Mims, W. B. *J. Magn. Reson.* **1984**, *59*, 291–306.
(78) Mims, W. B. , Electron Spin Echoes. In *Electron Paramagnetic Resonance*; Geschwind, S., Ed.; Plenum Press: New York, 1972; pp 263–351.

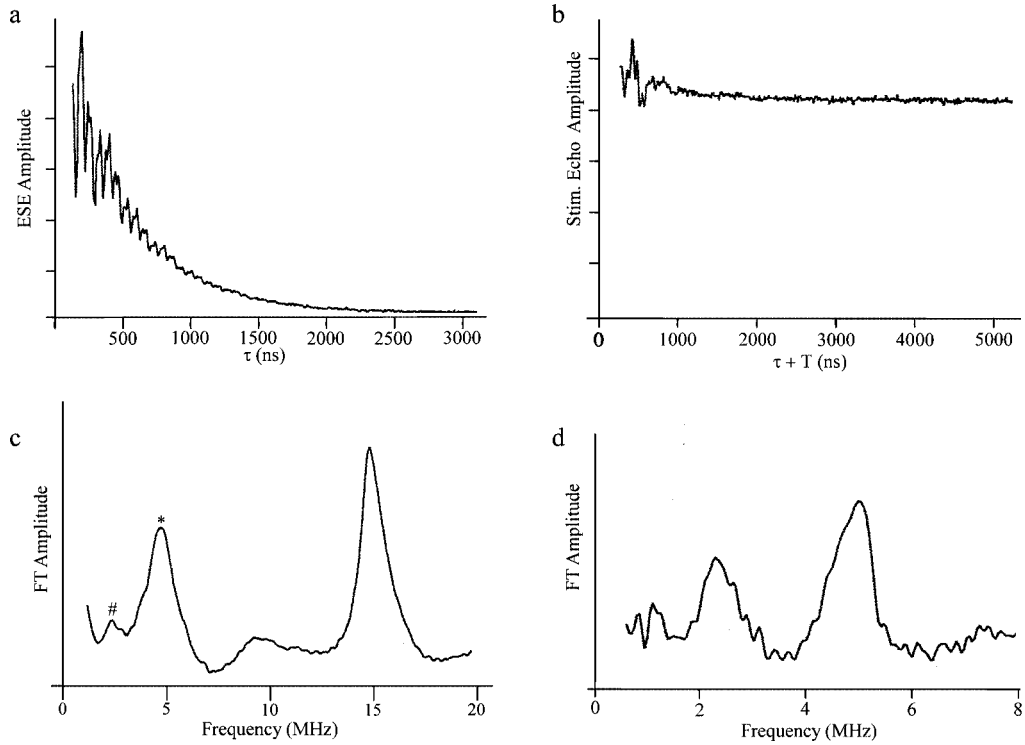

Figure 2. Two- and three-pulse X-band time-domain and complimentary Fourier transform spectra. Panels a and c show the two-pulse time-domain and FT spectra, respectively. Panels b and d show the three-pulse time-domain and FT spectra, respectively. Instrument settings. Two-pulse data: $\nu_{MW} = 9.5016$ GHz, $B = 0.3500$ T, $\pi/2$ pulse = 12 ns, $\Delta\tau = 10$ ns, repetition time = 5 ms, temperature = 4.2 K. Three-pulse data: same parameters as the two-pulse data but with $\tau = 268$ ns and $\Delta T = 15$ ns.

ments to be performed at the "multiline" signal absorption maximum without overlapping the contribution from $Y_D^{\bullet}$.

X- and P-Band ESEEM. Two- and three-pulse ESEEM spectra of the S_2 state were recorded at six microwave frequencies on the high-field side of $Y_D^{\bullet}$ at a constant g value of $g = 1.98$. Parts a and b of Figure 2 show representative X-band ($\nu_{MW} = 9.50$ GHz and $B = 0.3500$ mT) time-domain spectra for two- and three-pulse ESEEM, respectively. The corresponding frequency-domain spectra from Fourier analysis are shown in Figure 2c,d. The two-pulse frequency-domain spectra in Figure 2c clearly show the bound histidine ~5 MHz peak[3] (labeled *), a smaller positive feature at ~2 MHz (labeled #), as well as a negative feature at ~7 MHz. This negative feature may be a combination peak because two-pulse ESEEM spectra contain modulation frequencies that are combinations of the sums and differences of fundamental frequencies.[79] The dominant peak at 15 MHz, present in Figure 2c, is due to weakly coupled protons. The three-pulse time-domain spectra in Figure 2b show rather shallow modulation features that are completely damped out by ~1 μs. The τ value of 268 ns employed in this data set was chosen in order to suppress the weakly coupled proton modulation. The frequency-domain data in Figure 2d show broad frequency components at ~2.5 and ~5 MHz, as in the two-pulse ESEEM. However, there is no sign of the ~7 MHz peak. This is not surprising because the modulation frequencies in three-pulse ESEEM result from only fundamental frequencies, at least for a single nucleus.

(79) Kevan, L. ; Schwartz, R. N. *Modulation of Electron Spin-Echo Decay in Solids*; Wiley: New York, 1979; pp 241–279.

Table 1. Summary of X- to P-Band S_2-State Field Tracking

ν_{MW} (GHz)	B_0 (T)	g value
9.749	0.3525	1.98
10.995	0.3955	1.98
13.530	0.4875	1.98
15.517	0.5605	1.98

Because the line shapes and peak positions of the above data sets show no signs of sharp exact cancelation NQ frequencies, as described in eq 6, further ESEEM experiments were conducted over a range of X- and P-band microwave frequencies at constant g-value-constrained magnetic fields. These additional experiments were performed on the same pulsed EPR spectrometer, at the four higher microwave frequencies and magnetic fields listed in Table 1. Parts a and b of Figure 3 show the resulting frequency-domain spectra of these two- and three-pulse multifrequency experiments. The arrows in Figure 3a indicate the peak positions for the matrix proton frequencies, while the peaks marked with * and # correspond to the ^{14}N features. As in Figure 2c, Figure 3a shows a main feature at ~5 MHz and a shoulder at ~2.5 MHz. As the microwave frequency is increased to 15.5 GHz (0.5605 T trace in Figure 3a), the two ^{14}N peaks diverge, with a new shoulder feature appearing near 3.5 MHz. As well, the proton matrix resonance tracks to higher frequency, coincident with diminished intensity, according to the fact that the modulation depth is proportional to the inverse of the square of the magnetic field for such dipolar-coupled protons.[78] The low-frequency features attributed to HF-coupled ^{14}N nuclei exhibit independent field tracking behavior. A graphical linear least-squares analysis, in which the peak position is plotted against the nuclear

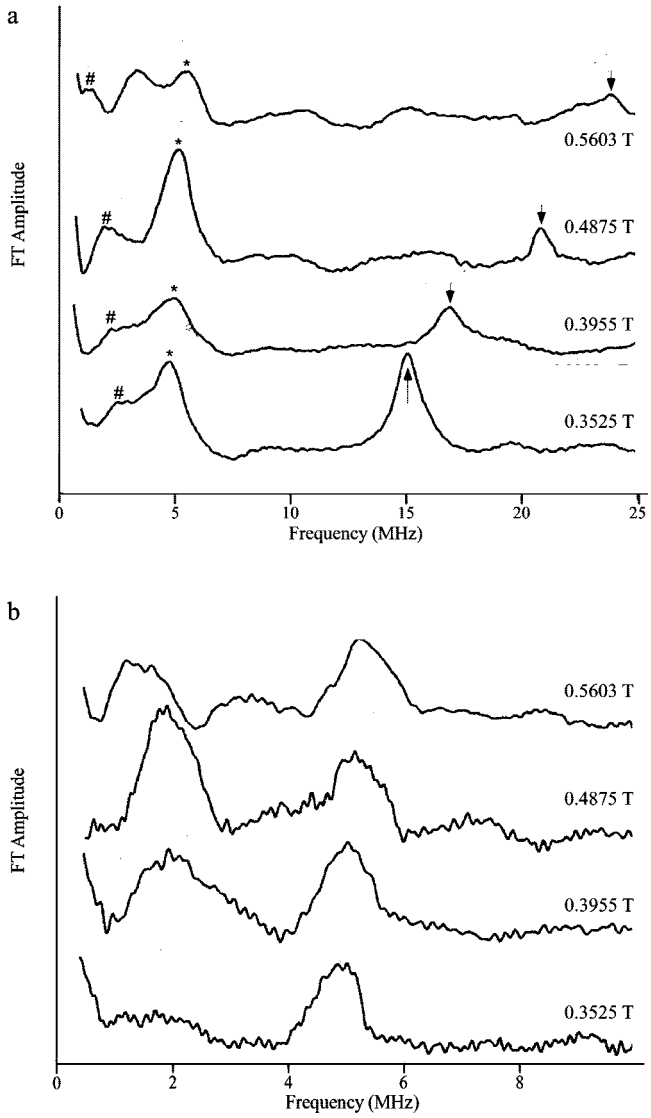

Figure 3. Two- and three-pulse X- to P-band ESEEM FT spectra. Panel a shows the two-pulse field tracking behavior. Panel b shows the three-pulse field tracking behavior. The microwave frequencies for each trace are listed in Table 1. The magnetic field positions for panels a and b are 0.3525, 0.3955, 0.4875, and 0.5605 T. The two-pulse data were acquired with the same instrumental parameters as those described in Figure 2. The τ values for each three-pulse experiment in panel b are 168 ns (0.5605 T), 193 ns (0.4875 T), 237 ns (0.3955 T), and 266 ns (0.3525 T).

Larmor frequency, allows us to differentiate between ν_{SQ} and ν_{DQ} transitions. From this (data not shown), the #-labeled low-frequency peak tracks to lower frequency as $-2\nu_I$, indicative of a ν_{DQ} transition. However, the higher frequency peak (*) tracks as $1\nu_I$, indicative of a ν_{SQ} transition. This same approach was used in analyzing the three-pulse ESEEM spectra in Figure 3b. Upon an increase in the incident microwave frequency from 9.75 to 15.52 GHz, the main feature (~5 MHz) tracks from 4.90 to 5.15 MHz, while the low-frequency component tracks from ~2 to ~1.8 MHz. The tracking behaviors of both sets of peaks show no indication that either tracks as a clear ν_{SQ} or ν_{DQ} transition. We note that the broad line shapes of these features change significantly as a function of the applied field strength. As such, the analysis may be limited by the lack of obvious peak maxima to monitor. Regardless, even with the ability to tune the microwave spectrometer over a 6 GHz range, the spectra from the X- and P-band instrument are still rather poorly resolved. However, the negative field tracking behavior of the low-frequency peaks in both the two- and three-pulse data in Figure 3 suggests that we are below the cancelation condition necessary to observe deeply modulated ESEEM data for a strongly HF-dominated ^{14}N coupling. In contrast, if we were above the cancelation condition, we would expect positive field tracking of all frequency peaks because the effective field in each spin manifold would be continuously additive.

K_a-Band ESEEM. Because the X- and P-band multifrequency ESEEM experiments provide no evidence of exact cancelation frequencies, further ESEEM studies were performed on a recently constructed K_a-band pulsed spectrometer.[76] Parts a and b of Figure 4 show the K_a-band two- and three-pulse time-domain data ($\nu_{MW} = 30.757$ GHz and $B = 1.1079$ T), respectively. The corresponding frequency-domain spectra from Fourier analysis are shown in Figure 4c,d. Additional ESEEM spectra were recorded at four other field positions and three τ values (data not shown). In this work, the displayed data sets only show spectra taken at a constant $g = 1.98$ and $\tau = 170$ ns (three-pulse data). Compared to the X- and P-band data above, time-domain spectra acquired at the K_a-band show significantly deeper modulation. This enhanced modulation translates to the well-resolved frequency-domain spectra presented in Figure 4c,d. The two-pulse ESEEM frequency-domain spectrum shown in Figure 4b has three positive features at 2.05, 6.58, and 13.84 MHz and two negative features at ~4.51 and ~8.52 MHz flanking the positive 6.58 MHz peak. These negative peaks arise from combinations of fundamental frequencies ν_a and ν_b and appear as $\nu_a \pm \nu_b$, $2\nu_{a(\beta)}$, etc.[79] Of important note in the two-pulse data is the lack of any weakly coupled proton frequency components. At the microwave frequencies and magnetic fields employed in these K_a-band experiments, such features would occur at >45 MHz. Thus, the scale in Figure 4c reflects the absence of such features. This is consistent with the multifrequency two-pulse data in Figure 3a that show diminished proton intensity with subsequent increased microwave frequency and magnetic field. Such an effect is advantageous in that there is no need to select τ values necessary for proton suppression in the three-pulse K_a-band ESEEM experiments. The three-pulse ESEEM spectra show deep modulation out to >4 μs, and the corresponding frequency-domain data (Figure 4d) show major spectral features at 0.88, 1.98, 6.90, and 14.00 MHz. The narrow, low-frequency components (<3 MHz) are suggestive of NQ transitions, while the 6.90 and 14.00 MHz frequencies are suggestive of ν_{SQ} and ν_{DQ} transitions, respectively. The general positions and line shapes of the K_a-band frequency-domain data indicate that we have indeed approached the cancelation condition with the new higher field spectrometer.

Simulations. The resolved NQ transitions apparent in the low-frequency region of the K_a-band three-pulse ESEEM spectrum allow for the approximation of e^2qQ and η directly. The presence of just two peaks (0.88 and 1.98 MHz) implies that $\eta \sim 1$. This condition corresponds to an equally spaced

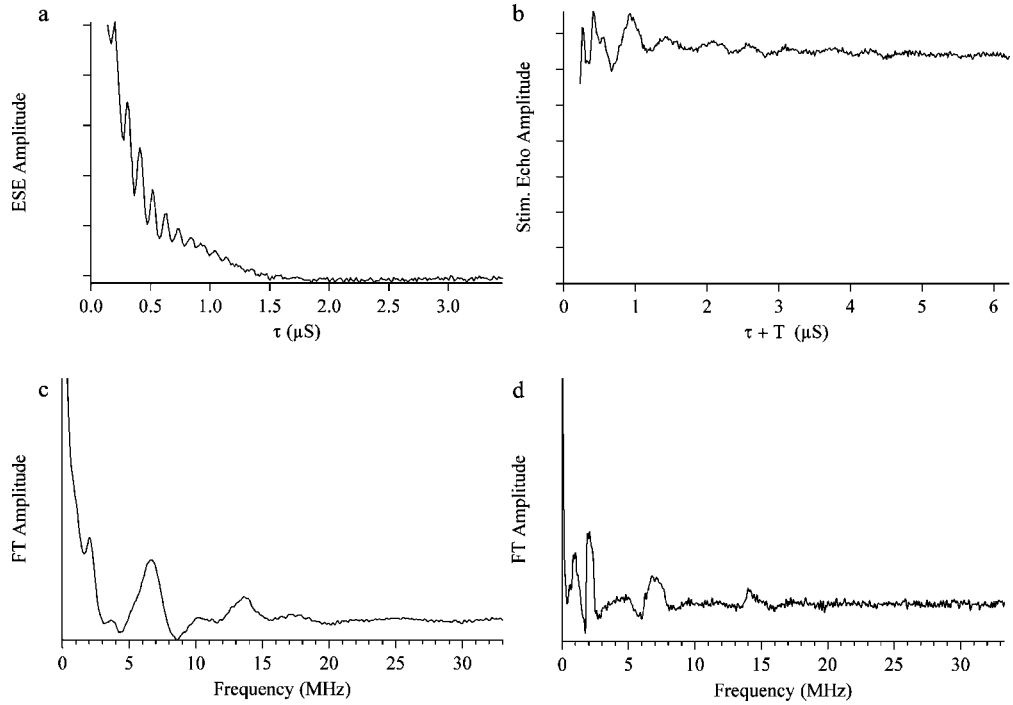

Figure 4. K_a-band ESEEM experiments at $g = 1.98$ (1.1079 T). Panel a shows the two-pulse ESEEM time-domain spectrum. Panel c shows the corresponding two-pulse frequency-domain spectrum. Panel b shows the three-pulse ESEEM time-domain specrum. Panel d shows the corresponding three-pulse ESEEM frequency-domain spectrum. Instrument settings: $\nu_{MW} = 30.757$ GHz, $\pi/2$ pulse = 10 ns, two-pulse $\Delta\tau = 15$ ns, three-pulse $\tau = 170$ ns, three-pulse $\Delta T = 15$ ns, repetition time = 5 ms, temperature = 4.5 K.

set of NQ energy levels; thus, we preliminarily assign the feature at 0.88 MHz to the overlapping ν_0 and ν_- transitions. The peak at 1.98 MHz, nearly twice that of the 0.88 MHz peak, is thus assigned to the ν_+ NQ transition. Using these transition frequencies in conjunction with eq 5 gives our estimate for e^2qQ of ~2 MHz. By attributing the peak at ~14 MHz to the ν_{DQ} transition of the same nucleus responsible for the NQ transitions, we can calculate an estimate for α_{iso} of ~7 MHz using eq 6.

Equations 5 and 6 are strictly valid when $\alpha_{dip} \sim 0$ MHz, an unlikely condition given the large magnitude of α_{iso} and the assumed proximity of the corresponding nucleus to the center of the unpaired electron spin. Therefore, we have used the above-derived values of η, e^2qQ, and α_{iso} only as initial inputs for our spectral simulations and included the additional parameter α_{dip}, which was allowed to vary from 0.5 to 2.0 MHz. Of importance to note is the fact that no peaks from combinations of zero-field NQ frequencies are apparent in the three-pulse data, which would indicate the presence of multiple equivalent ^{14}N nuclei. With this in mind, the starting simulations assume one nitrogen contribution, an axially symmetric HF contribution, and a relatively strong NQ interaction with a high asymmetry parameter.

The best-fit simulations are compared to the two- and three-pulse K_a-band ESEEM spectra in parts a and b of Figure 5, respectively. These simulations were achieved using the spin-Hamiltonian parameters: $\alpha_{iso} = 7.30 \pm 0.20$ MHz, $\alpha_{dip} = 0.50 \pm 0.10$ MHz, $e^2qQ = 1.98 \pm 0.05$ MHz, and $\eta = 0.84 \pm 0.06$. Varying each of the four simulation parameters and visually inspecting the resulting frequency-domain spectra determined the estimated errors in the simulations. The two-pulse simulations are in excellent agreement with the experimental spectra with respect to the overall peak positions, with only slight line-shape and intensity differences. The low-frequency region (<5 MHz) of the simulated data of Figure 5a shows clear peaks at ~1 and 2 MHz. The 2 MHz peak is consistent with the experimental data, while the lower frequency (~1 MHz) peak is not resolved; however, a slight shoulder is evident. Additionally, the simulation shows intense peaks at ~7 and ~14 MHz consistent with the experimental data. In the three-pulse ESEEM spectrum (Figure 5b), our simulations clearly reproduce all peak positions and relative line shapes. Again, however the intensities are slightly different. The 14 MHz peak shows greater amplitude in the simulation, while the low-frequency NQ frequencies exhibit opposite intensity profiles. Of particular importance is that the simulation confirms the presence of at least one ν_{SQ} transition at 7 MHz. Given that this frequency component is half the ν_{DQ} peak (14 MHz) and that $\eta \cong 1$, it seems likely that the two possible ν_{SQ} frequencies are nearly degenerate and thus indistinguishable from each other. At X-band frequencies, these transitions are strongly orientation-dependent and are generally broadened beyond observation. However, Flanagan and Singel have shown that resolution of such single-quantum transitions is possible when the ratio of e^2qQ to $4\nu_I$ is less than 0.30.[67] Such is the case in these K_a-band experiments, where this ratio is 0.14. An additional feature in both the simulated and experimental data is a broad peak centered at ~4 MHz. This component was determined through simulation to be an artifact that results from imperfect "dead-time" reconstruction. Specifically, this feature is not present unless a simulated "dead time" is introduced into the simulated time-domain spectrum.

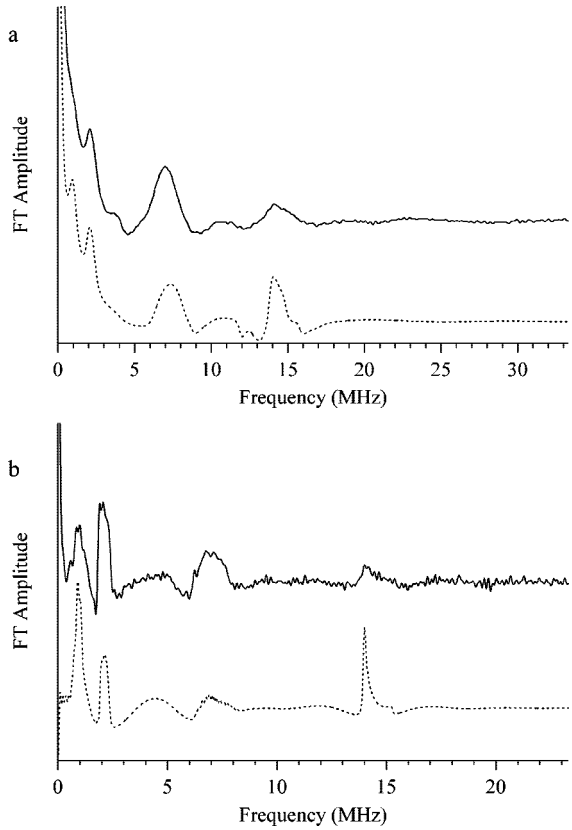

Figure 5. K_a-band two- and three-pulse ESEEM simulations. Panel a shows the two-pulse frequency-domain spectra, and panel b shows the three-pulse frequency-domain spectra. The experimental data are the solid trace, and the simulated data are the dashed trace. Simulation parameters: $B = 1.1070$ T, $\alpha_{iso} = 7.3$ MHz, $\alpha_{dip} = 0.5$ MHz, $e^2qQ = 1.98$ MHz, $\eta = 0.88$, and $\tau = 170$ ns for the three-pulse simulation.

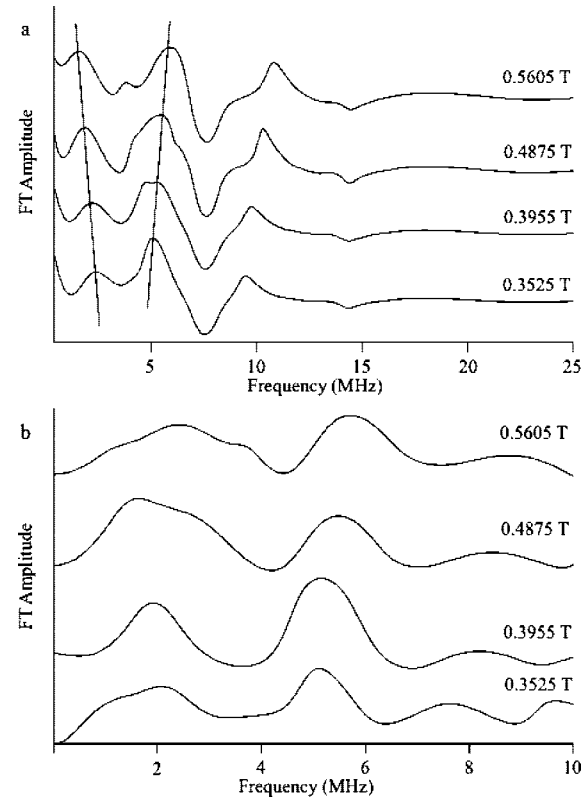

Figure 6. X- to P-band two- and three-pulse ESEEM simulations. Panel a shows the two-pulse frequency-domain spectra, and panel b shows the three-pulse frequency-domain spectra. The simulation parameters are the same as those in Figure 5, and the magnetic field and τ values correspond to those in Figure 3.

Additional two- and three-pulse simulations, with the identical input parameters above, were employed to fit the lower-frequency ESEEM data. Figure 6 shows the corresponding X- to P-band frequency-domain simulations for comparison with Figure 3. The two-pulse simulations in Figure 6a show excellent agreement with the experimental data in the low-frequency (<6 MHz) portion of Figure 6a. The ~2 MHz peak observed at the X band shifts to lower frequency (~1.5 MHz), while the ~5 MHz peak shifts to higher frequency (~5.5 MHz) with subsequent resolution of a lower-frequency shoulder at ~3.5 MHz. Trend lines in Figure 6a indicate these shifts. However, the higher-frequency regions (>6 MHz) of the simulations show resolved combination peaks (negative features at ~7 and ~14 MHz) and a double-quantum peak at ~10 MHz that are unresolved in the experimental data. The three-pulse simulations (Figure 6b) are not complicated by such combination peaks and show a qualitatively better match to the experimental data. The major spectral features of the experimental data are well reproduced in these simulations. There is a slight shift to higher frequency in the ~5 MHz peak and a low-frequency shift in the ~2 MHz peak with subsequent broadening of both spectral components. Such a strong correlation between the simulations and multifrequency experimental data importantly shows that the majority of the low-frequency (X- to P-band) modulation results from the same ^{14}N nucleus that is well-resolved at K_a-band frequencies. However, we cannot rule out the possibility that some differences between the simulations and X- to P-band experimental spectra may be due to additional contributions from one or more weakly coupled ^{14}N nuclei.

Discussion

The K_a-band ESEEM results demonstrate a dramatic improvement in the spectral resolution of ^{14}N HF and NQ transitions, compared to the X- and P-band results. Deep modulation patterns persist to >4 μs, and well-resolved NQ frequencies are present at 0.88 and 1.98 MHz. Also, the K_a-band experiments resolve features at 6.9 and 14.0 MHz, which are ascribed to the ν_{SQ} and ν_{DQ} transitions of the same ^{14}N nucleus that gives rise to the NQ transitions described above. Indeed, our simulations of the K_a-band two- and three-pulse data almost completely reproduce all observed spectral features using HF and NQ coupling constants from a single ^{14}N nucleus. The derived spin-Hamiltonian parameters, $\alpha_{iso} = 7.3 \pm 0.20$ MHz and $\alpha_{dip} = 0.50 \pm 0.10$ MHz, confirm that the ^{14}N nucleus is strongly coupled to the OEC. As well, the NQ coupling values ($e^2qQ = 1.98 \pm 0.05$ MHz and $\eta = 0.84 \pm 0.06$) are consistent with histidine ^{14}N NQ values measured in superoxidized manganese catalase from *Lactobacillus plantarum* ($e^2qQ = 2.19$ MHz and $\eta = 0.58$).[80]

(80) Stemmler, T. L.; Sturgeon, B. E.; Randall, D. W.; Britt, R. D.; Penner-Hahn, J. E. *J. Am. Chem. Soc.* **1997**, *119*, 9215–9225.

Using this same parameter set, we are able to simulate the experimental data trends of two- and three-pulse data acquired at five frequencies between the X- and P-bands. Specifically, the two-pulse simulations show a downshift of the broad ~2.0 MHz peak at 0.3525 T to ~1.5 MHz at 0.5605 T, as well as a splitting of the ~5 MHz peak at 0.3525 T into two components at 0.5605 T. As well, the three-pulse simulations show a slight upshift in the ~5 MHz peak and a downshift of the ~2 MHz peak, consistent with the experimental data. However, there are slight differences between the experimental and simulated data sets. One possible explanation can be related to the mathematical treatment of the simulated data sets. In both the two- and three-pulse simulations, a single-exponential damping function, with a time constant determined from the experimental data, was applied to the modulated component of the time-domain spectrum. Such a global exponential fitting may not, in fact, be completely adequate because individual modulation components may damp differently because of various line-broadening mechanisms (i.e., strain in quadrupolar vs HF tensors). As such, the relative amplitudes of individual frequency-domain components may not be properly reproduced. However, it is possible that additional weakly coupled ^{14}N nuclei also contribute to the modulation observed in the lower-frequency instrument. Such a weakly coupled ^{14}N nucleus (isotropic HF coupling, $\alpha_{iso} \ll 1$ MHz) would generate two peaks corresponding to double-quantum nuclear transitions in the frequency-domain spectra.[67] A very weak coupling would give rise to shallow modulations even at the lowest microwave frequencies and magnetic fields employed in this study. These features could be buried under the broad-frequency components arising from the ^{14}N nucleus with the larger HF interaction.

If the strongly coupled nitrogen is indeed from the directly coordinated ^{14}N nucleus of histidine, it should indeed be accompanied by a weaker coupling from the noncoordinating remote nitrogen of the histidine imidazole ring. For example, in blue copper proteins such as azurin and in model copper imidazole complexes, the isotropic HF coupling of the directly bound nitrogen of histidine or imidazole is ~20 times that of the remote nitrogen.[81–85] A similar relationship has been shown for direct and remote ^{14}N HF interactions in oxovanadium (VO^{2+}) model complexes with histidine and imidazole ligands, as well as in metalloproteins, where VO^{2+} serves as a spin probe of the enzyme active site.[86–88] In other metalloenzymes with dinuclear iron centers such as Reiske proteins, methanmonooxygenase, and methemerythrin, the ^{14}N HF interaction for the directly coordinated histidine nitrogen is ~10–16 times that of the remote histidine nitrogen.[89–91]

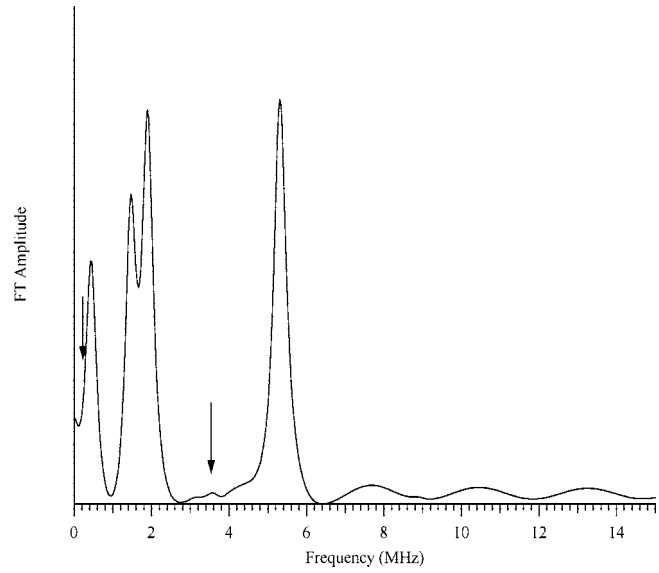

Figure 7. Simulated composite X-band three-pulse ESEEM frequency-domain spectrum for the ^{14}N HF couplings detected by Tang et al. in ref 48.

A previous X-band CW-ENDOR study of ^{14}N- and ^{15}N-labeled PSII particles from *Synechococcus el.* reported two ^{15}N HF (3.7 and 0.7 MHz) couplings suggestive of two distinct N atoms directly coordinated to the OEC.[48] Scaling these values by the ratio of the γ values of ^{14}N to ^{15}N ($^{14}\gamma/^{15}\gamma = 0.71$) gives the corresponding isotropic ^{14}N HF values of 2.6 and 0.7 MHz. The larger (2.6 MHz) HF value is near the cancelation limit at the X-band microwave frequencies and magnetic field range explored in the current study. As such, we would expect to detect deep modulation in the time-domain spectrum that corresponds to the strong frequency-domain spectra shown in the simulated spectrum of Figure 7. (Simulation parameters. Nitrogen 1: $\alpha_{iso} = 0.70$ MHz, $\alpha_{dip} = -0.10$ MHz, $e^2qQ = 2.2$ MHz, $\eta = 0.4$. Nitrogen 2: $\alpha_{iso} = 2.60$ MHz, $\alpha_{dip} = -0.10$ MHz, $e^2qQ = 2.2$ MHz, $\eta = 0.4$. In both simulations, $g = 1.98$, $B = 0.3525$ T, and $\tau = 266$ ns. The simulation is fit with a single-exponential damping function with a time constant of 1 μs.) We note that the simulated spectrum in Figure 7 was generated using the ^{14}N HF values described by Tang et al. and typical histidine NQ values. The weaker (0.7 MHz) coupling is well below the cancelation condition for any of the employed magnetic fields in the current study. However, in the absence of large HF anisotropies, characteristic double-quantum frequency components would be expected at the positions

(81) Mims, W. B.; Davis, J. L.; Peisach, J. *J. Magn. Reson.* **1990**, *86*, 273–292.
(82) Mims, W. B.; Peisach, J. *J. Chem. Phys.* **1978**, *69*, 4921–4930.
(83) Coremans, J. W. A.; Poluektov, O. G.; Groenen, E. J. J.; Canters, Q. W.; Nar, H.; Messerschmidt, A. *J. Am. Chem. Soc.* **1996**, *118*, 12141–12153.
(84) Coremans, J. W. A.; van Gastel, M.; Poluektov, O. G.; Groenen, E. J. J.; den Blaawuen, T.; van Pouderoyen, G.; Canters, Q. W.; Nar, H.; Hammann, C.; Messerschmidt, A. *Chem. Phys. Lett.* **1995**, *235*, 202–210.
(85) Coremans, J. W. A.; Poluektov, O. G.; Groenen, E. J. J.; Canters, Q. W.; Nar, H.; Messerschmidt, A. *J. Am. Chem. Soc.* **1997**, *119*, 4726–4731.
(86) Dikanov, S. A.; Burgard, C.; Huttermann, J. *Chem. Phys. Lett.* **1993**, *212*, 493–498.
(87) Dikanov, S. A.; Samoilova, R. I.; Smieja, J. A.; Bowman, M. K. *J. Am. Chem. Soc.* **1995**, *117*, 10579–10580.
(88) Gerfen, G. J.; Hanna, P. M.; Chastenn, N. D.; Singel, D. J. *J. Chim. Phys. Phys.-Chim. Biol.* **1991**, *113*, 9513–9519.
(89) Hendrich, M. P.; Fox, B. G.; Anderson, K. K.; Debrunner, P. G.; Lipcomb, J. D. *J. Biol. Chem.* **1992**, *267*, 261–269.
(90) Gurbiel, R. J.; Doan, P. E.; Gassner, G. T.; Macke, T. J.; Case, D. A.; Ohnishi, T.; Fee, J. A.; Ballou, D. P.; Hoffman, B. M. *Biochemistry* **1996**, *35*, 7834–7845.
(91) Dikanov, S. A.; Davydov, R. M.; Graslund, A.; Bowman, M. K. *J. Am. Chem. Soc.* **1998**, *120*, 6797–6805.

labeled with arrows in Figure 7. While our multifrequency X- to P-band data show no indication of the 2.6 MHz coupling, Figure 7 suggests that the 0.7 MHz coupling may be below the detection limit of the instrument employed in this study. As such, lower-frequency ESEEM experiments would be necessary to verify the existence of a weaker ^{14}N HF coupling, and thus we cannot disregard the probability of such.

The S_2 state is composed of four spin-coupled Mn^{III} and Mn^{IV} ions. While there remains some debate as to whether the oxidation-state composition of the S_2 state is $(Mn^{III})_3Mn^{IV}$ or $Mn^{III}(Mn^{IV})_3$, the most compelling evidence points toward the latter.[7–10,24,28,33,40,41,92–95] We therefore adopted the $Mn^{III}(Mn^{IV})_3$ model and compare the detected HF and NQ values to previously reported ^{14}N ligand HF and NQ values in dinuclear $Mn^{III}Mn^{IV}$ model compounds, imidazole-coordinated metal complexes, and histidine imidazole nitrogens coordinated by the dinuclear $Mn^{III}Mn^{IV}$ center of superoxidized manganese catalase. We divide further analysis into HF and NQ comparisons.

A previous nuclear quadrupolar resonance (NQR) study of zinc and cadmium imidazole compounds determined a range (1.9–3.2 MHz) of e^2qQ and η (0.70–0.13) values for imidazole imino nitrogen interactions.[96] Because of similar electronic environments of nitrogens in imidazole and the imidazole ring of histidine, we can relate our determined NQ values to those determined by NQR. As such, our e^2qQ (1.98 ± 0.05 MHz) values are within the range of the NQR studies while our asymmetry parameter ($\eta = 0.84 \pm 0.06$) is significantly larger. Such differences in η may be expected because the asymmetry of the electric field gradient is extremely sensitive to slight changes in the local structure. This is clearly shown in the wide range of η values determined by the NQR experiments across relatively similar classes of metal-histidine coordination compounds.[96] The most relevant system for comparing the NQ values is that of superoxidized manganese catalase. A previous X- to P-band ESEEM study of this enzyme detected a single ^{14}N coupling associated with a histidine imidazole nitrogen coordinated to the dinuclear $Mn^{III}Mn^{IV}$ active site.[80] The NQ values ($e^2qQ = 2.19$ MHz and $\eta = 0.58$) detected in the native enzyme are perturbed by cyanide and azide inhibition of the enzyme. Inhibition of the enzyme resulted in a decrease in the ^{55}Mn HF couplings of both Mn ions and thus an increase of the spin density on the histidine ligand. The ^{14}N histidine imidazole NQ values for azide ($e^2qQ = 1.97$ MHz and $\eta = 0.74$) and cyanide ($e^2qQ = 1.93$ MHz and $\eta = 0.74$) inhibited manganese catalase are consequently comparable to the values detected in this study. It is important to note that X-ray crystallographic studies of manganese catalase single crystals show two histidine residues coordinated to the dinuclear manganese center.[97–101] The second histidine interaction has thus far escaped spectroscopic detection, and therefore no information regarding HF and NQ couplings is available. Regardless, such comparable ESEEM-detected NQ values are consistent with a histidine nitrogen bound to the manganese cluster of the OEC.

In a similar manner, the determined ^{14}N isotropic HF value ($\alpha_{iso} = 7.3 \pm 0.20$ MHz) may be compared to literature values for α_{iso} values of nitrogens bound to dinuclear $Mn^{III}Mn^{IV}$ cores. A number of such model compounds with nitrogen coupling from ligands such as bypyridine, 1,4,8,11-tetraazacyclotetradecane, tris(2-methylpyridyl)amine, 1,2-bis(1,4,7-triaza-1-cyclononyl)ethane, 1,10-phenanthroline, and *N*,*N*′-bis(2-pyridylmethyl)ethane-1,2-diamine have been investigated with CW-ENDOR, pulsed ENDOR, and ESEEM.[102–106] From these experiments, two classes of nitrogen HF couplings were detected: a strong HF coupling with α_{iso} ranging from 9 to 12 MHz and a weaker coupling with α_{iso} ranging from 2 to 5 MHz. The strong couplings were assigned to nitrogen axially coordinated to a Mn^{III} ion, while the weaker couplings were assigned to nitrogens equatorially coordinated to either a Mn^{III} or Mn^{IV} ion. We note that there is no precedent to distinguish between axial or equatorial coordination to a Mn^{IV} ion, and thus the small HF couplings could be assigned to either position. The HF value ($\alpha_{iso} = 7.3 \pm 0.20$ MHz) determined in the present study is intermediate within this range of strongly and weakly coupled ^{14}N in $Mn^{III}Mn^{IV}$ dinuclear compounds.

To assign an observed ^{14}N HF coupling to a specific valence of the Mn−N unit (e.g., Mn^{III}−N vs Mn^{IV}−N), one must project out the site-specific Mn HF coupling values using the spin projection factor for the coordinating Mn ion. For example, for the binuclear $Mn^{III}Mn^{IV}$ clusters (assuming approximately equal intrinsic HF interaction, small zero-field splitting, and large exchange interaction),[28,107,108] a measured ligand HF coupling to a Mn^{III} ion would be twice as large as one to a Mn^{IV} ion because the spin projection factors are

(92) Yachandra, V. K.; Sauer, K.; Klein, M. P. *Chem. Rev.* **1996**, *96*, 2927–2950.
(93) Penner-Hahn, J. E. Structural Characterization of the Mn Site in the Photosynthetic Oxygen-Evolving Complex. In *Metal Sites in Proteins and Models: Redox Centres*; Hill, H. A. O., Sadler, P. J., Thompson, A. J., Eds.; Springer: Berlin, 1998; Vol. *90*, pp 1–36.
(94) Riggs, P. J.; Yocum, C. F.; Penner-Hahn, J. E.; Mei, R. *J. Am. Chem. Soc.* **1992**, *114*, 10650–10651.
(95) Iuzzolino, L.; Dittmer, J.; Dorner, W.; Meyer-Klaucke, W.; Dau, H. *Biochemistry* **1998**, *37*, 17112–17119.
(96) Ashby, C. I. H.; Cheng, C. P.; Brown, T. L. *J. Am. Chem. Soc.* **1978**, *100*, 6057–6063.
(97) Barynin, V. V.; Hempstead, P. D.; Vagin, A. A.; Antonyuk, S. V.; Melik-Adamyan, W. R.; Lamzin, V. S.; Harrison, P. M.; Artymiuk, P. J. *J. Inorg. Biochem.* **1997**, *67*, 196.
(98) Whittaker, M. M.; Barynin, V. V.; Antonyuk, S. V.; Whittaker, J. W. *Biochemistry* **1999**, *38*, 9126–9136.
(99) Antonyuk, S. V.; Melik-Adamyan, V. R.; Popov, A. N.; Lamzin, V. S; Hempstead, P. D.; Harrison, R. M.; Artymyuk, P. D.; Barynin, V. V. *Kristallografiya* **2000**, *45*, 111–122.
(100) Barynin, V. V.; Whittaker, M. M.; Antonyuk, S. V.; Lamzin, V. S.; Harrison, P. M.; Artymiuk, P. J.; Whittaker, J. W. *Structure* **2001**, *9*, 725–738.
(101) Whittaker, M. M.; Barynin, V. V.; Igarashi, T.; Whittaker, J. W. *Eur. J. Biochem.* **2003**, *270*, 1102–1116.
(102) Randall, D. W. Ph.D. Thesis, University of California, Davis, Davis, CA, 1997.
(103) Randall, D. W.; Chan, M. K.; Armstrong, W. H.; Britt, R. D. *Mol. Phys.* **1998**, *95*, 1283–1294.
(104) Schaefer, K.-O.; Bittl, R.; Zweygart, W.; Lendzian, F.; Haselhorst, G.; Weyhermueller, T.; Wieghardt, K.; Lubitz, W. *J. Am. Chem. Soc.* **1998**, *120*, 13104–13120.
(105) Tan, X. L.; Gultneh, Y.; Sarneski, J. E.; Scholes, C. P. *J. Am. Chem. Soc.* **1991**, *113*, 7853–7858.
(106) Khangulov, S. V.; Sivaraja, M.; Barynin, V. V.; Dismukes, G. C. *Biochemistry* **1993**, *32*, 49124924..
(107) Gerritsen, H. J.; Sabisky, E. S. *Phys. Rev.* **1963**, *132*, 1507–1512.
(108) Andresen, H. G. *Phys. Rev.* **1960**, *121*, 1606–1611.

Table 2. Range of Site-Specific ^{14}N HF Couplings Calculated from the Manganese Cluster Spin Projection Factors of Reference 41

Mn ion	A_{iso} (MHz)	A_{dip} (MHz)	R (Å)
Mn^{III}	3.65–9.69	0.23–0.59	2.92–2.13
Mn^{IV}	5.44–11.23	0.33–0.69	2.60–2.00

+2 for Mn^{III} and −1 for Mn^{IV}. The predicted projection factors for the manganese cluster in the OEC range from 0.76 to 2 for Mn^{III} and from 0.65 to 1.34 for Mn^{IV} (depending on the which Mn ions are in a 3+ or 4+ oxidation state).[40] By scaling the effective ^{14}N HF values determined above by the limits of these projection factors, we obtain the range of HF values (labeled A_{iso} and A_{dip}) as shown in Table 2. Of particular note are the values for the Mn^{IV} ion. The calculated A_{iso} values in Table 2 appear to be inconsistent with any literature precedent for either axially or equatorially coordinated nitrogen. However, the range of HF values for the Mn^{III} ion, along with an e^2qQ value of ~2 MHz, are within those of the literature for nitrogen equatorially coordinated to Mn^{III}, as mentioned above.[48,96,104,105] It should be noted that the distances calculated with respect to A_{dip} in Table 2 are limited by the point-dipole approximation. Because the unpaired electron spin neither is on one central Mn metal ion nor distributed symmetrically over the atoms of the manganese cluster, this approximation serves only as a qualitative measure of the electron ^{14}N nuclei distance.

This argument for histidine ligation is in agreement with previous EPR and mutagenesis studies that show that His-332 is necessary for efficient photoassembly of the manganese cluster,[14] as well as proper *S*-state turnover.[12,16,109] Further evidence that His-332 is directly coordinated to the manganese cluster is provided by ESEEM studies of the His-332E mutant.[18] This study showed that the ~5 MHz feature in the 9 GHz two-pulse time-domain ESEEM spectrum essentially disappears in the His-332E mutant. In addition to the above data, X-ray crystallographic data of PSII have proposed histidine residues near the electron-density pocket of the manganese cluster.[9,10] While the exact structure of the manganese cluster is still unknown, recent polarized extended X-ray absorption fine structure and X-ray diffraction experiments were done to reassess the proposed structure of the manganese cluster.[24] In these new proposed structures, His-332 lies within the first coordination sphere of the manganese cluster. Further K_a- and Q-band ESEEM and ENDOR experiments on globally labeled ^{15}N and globally labeled ^{15}N with the histidine residues labeled ^{14}N PSII samples from *Synechocystis* are currently being explored. We believe these additional experiments will help further characterize the single ^{14}N interaction detected in this study.

Acknowledgment. We acknowledge the National Institute of Health (Grants GM 48242 and GM 66136) for financial support, CalEPR at University of California, Davis, and Dr. Troy A. Stich for helpful discussion and editing.

IC701680C

(109) Chu, H.-A.; Nguyen, A. P.; Debus, R. J. *Biochemistry* **1995**, *34*, 5859–5882.